communications materials

A Nature Portfolio journal

Article

https://doi.org/10.1038/s43246-026-01072-6

Manifold of magnetic nodal lines in an elemental ferromagnet

O. J. Clark[1,2], M. Garcia-Diez[3,4], J. Fink[5,6], O. Rader[1], R. Miranda[7], M. G. Vergniory[3,8,9] & J. Sánchez-Barriga[1,7]

Magnetic nodal line semimetals, defined by twofold degenerate gapless crossings along extended momentum paths, offer significant potential for spintronics and future information technologies. Despite their potential, these systems are rare in nature, with only few examples known to date. Here, using spin- and angle-resolved photoemission spectroscopy and density functional theory-based calculations, we classify ferromagnetic hexagonal close-packed (hcp) cobalt as a prototypical system exhibiting these properties. We demonstrate that manifolds of magnetic gapless nodal rings enclosing the Γ and K points in the $k_z = 0$ plane, and magnetic nodal lines spanning the entire A-L path in the $k_z = \frac{\pi}{c}$ plane, coexist and dominate the fermiology of this elemental system. These mirror-protected bulk crossing points are associated with surface states, both of which exhibit controllable spin textures. This work is the first identification of cobalt as a simple, yet highly tunable and rich topological platform for exploring and manipulating spin-polarised Weyl-like nodal lines at room temperature.

Topological nodal-line semimetals host band crossings that give rise to quasiparticles without direct counterparts in high-energy physics, unlike the Dirac and Weyl fermions found in point-node semimetals. These materials have been extensively studied using angle-resolved photoemission spectroscopy (ARPES), which provides direct insight into their momentum-resolved electronic structure and topological features[1]. Beyond their fundamental significance, nodal-line crossings can also lead to a range of emergent phenomena with potential relevance for next-generation electronic and spintronic applications. In systems with broken time-reversal symmetry (TRS), these include enhanced anomalous Hall effects and unconventional magnetotransport signatures[2–4].

Dirac nodal-line semimetals are relatively common place[5–14], typically employing non-symmorphic symmetry to stablise fourfold degenerate crossing points over extended paths in momentum space[9,15–29]. Twofold degenerate nodal lines in three-dimensional systems, however, are less common, and rely on either a breaking of inversion symmetry or TRS to lift the spin degeneracy strictly maintained in Dirac semimetals, while retaining sufficient symmetry constraints to ensure that gapless crossings are enforced[2,11,30–34]. The type of symmetry broken alters the spin structure of nodal lines: Where TRS is present, all band crossings at time-reversal-invariant-momenta are enforced to be spin degenerate, resulting in a reversal of spin polarisation between pairs of generic ± k-points. In contrast, magnetic systems in which TRS is broken can exhibit spin-polarised bands at any *k*-point, and thus carry a net spin-polarisation over the entire system. The ability to traverse ferromagnetic phase transitions and to controllably reverse spin-textures of both the nodal lines and any associated surface states through external magnetisation is exclusively possible in the TRS-broken subset of nodal-line systems. Moreover, the presence and size of the spin-orbit coupling (SOC) induced band gap can be tuned in three-dimensional systems by breaking the alignment of spin and orbital angular momentum through spin-reorienting magnetic fields, with Fe_3GeTe_2 as one of the few examples known to date[2]. Beyond Fe_3GeTe_2, magnetic nodal-line semimetals are relatively rare in nature[33–40], and direct observation of magnetic Weyl nodal lines with controllable spin textures in simple ferromagnetic systems remains elusive.

Here, we uncover the first elemental topological nodal-line system, realized in ferromagnetic hexagonal close-packed (hcp) cobalt. Through spin- and angle-resolved photoemission (spin-ARPES) and first principles calculations, we demonstrate how this strongly-correlated ferromagnet possesses an abundance of mirror-symmetry protected crossing points across the entire bulk Brillouin zone and over large energy ranges, including at the Fermi level. The types of nodal features found within this elemental ferromagnet fall into two distinct categories depending on the local symmetries of the two-dimensional $k_x - k_y$ plane in which they are found. In the

---

[1]Helmholtz-Zentrum Berlin für Materialien und Energie, Berlin, Germany. [2]Diamond Light Source, Harwell Science and Innovation Campus, Didcot, UK. [3]Donostia International Physics Center, Donostia-San Sebastian, Spain. [4]Physics Department, University of the Basque Country (UPV/EHU), Bilbao, Spain. [5]Leibniz Institute for Solid State and Materials Research Dresden, Dresden, Germany. [6]Institut für Festkörperphysik, Technische Universität Dresden, Dresden, Germany. [7]IMDEA Nanoscience, Madrid, Spain. [8]Département de Physique et Institut Quantique, Université de Sherbrooke, Sherbrooke, QC, Canada. [9]Regroupement Québécois sur les Matériaux de Pointe (RQMP), Montreal, QC, Canada. ✉e-mail: jaime.sanchez-barriga@helmholtz-berlin.de

k_z=0 (Γ) plane, rings of twofold degeneracies enclose the Γ point of the bulk Brillouin zone. In the $k_z = \frac{\pi}{c}$ (A) plane, spin-polarised nodal lines of twofold degenerate crossings points span the entire A-L-A line. In each case, these crossing points are gapless in the presence of SOC. Special attention is given to the nodal rings and lines at the Fermi level. All observed features are minority-spin states whose spin-direction can be manipulated with external magnetic fields, while the associated majority-spin partners are quenched due to spin-dependent electron-electron correlation effects[41–44].

The magnetic space group of hcp cobalt in which these nodal features are found is identical to that of Fe_3GeTe_2, and therefore one can expect further tunability through small perturbations from the nominal magnetization axis to generate topological charge[2]. However, the simple elemental composition removes issues with material fabrication, and a high Curie temperature ensures that these magnetic nodal crossings robustly exist at room temperature. Together, this work classifies hcp cobalt as a topological ferromagnet with transport dominated by spin-polarised Weyl-like charge carriers. Our present findings offer a paradigm shift in our current understanding of the band structure of ferromagnets and are important in the context of future applications for nodal-line systems in spintronics.

Results and discussion

Symmetry-permitted nodal features in hcp cobalt

First, we provide a comprehensive overview of the symmetry-protected nodal features with support from first-principles theoretical calculations. In Fig. 1a, the bulk and surface Brillouin zones (BBZ and SBZ, respectively) are displayed for hcp cobalt. There are two possible inequivalent magnetization axes, with the relative energetic preference dependent on material thickness[43]. An out-of-plane (|| c) magnetization axis corresponding to the Γ-A direction in momentum space preserves the in-plane three-fold rotational symmetry of the lattice, while the easy axis parallel to the Co[$1\bar{1}00$] direction ensures that the three Γ-M directions become inequivalent.

The types of nodes in cobalt are a product of the high-symmetry plane considered and the magnetisation direction, both of which alter the local symmetries which confine electronic behavior. Here, our high-quality bulk Co(0001) films possess two high symmetry momentum planes in k_z: $k_z = 0$ (Γ-containing plane), and $k_z=\frac{\pi}{c}$ (A-containing plane), shown in Fig. 1(a).

For a magnetization along the c-axis of the hexagonal structure, the precise symmetry description of the electronic eigenstates is given by the magnetic space group P6_3/mm'c' (No.194.279 in the Belov-Neronova-Smirnova notation[45]). The momentum subset (k_x, k_y, k_z = 0, 1/2) in fractional coordinates is generated only by translations along vectors of the lattice and the mirror plane with Seitz symbol $\{m_{001}|0, 0, 1/2\}$. The states on these planes can be separated into two different irreducible co-representations with mirror eigenvalues $\pm i$. As a consequence, hybridization between bands of different symmetry is forbidden and nodal lines can generically arise.

The resultant scenario for the Γ-containing plane (k_x, k_y, k_z = 0) is sketched in Fig. 1(b) and supported by density functional theory (DFT) calculations in Fig. 2. Arrays of crossing points between bands with different mirror eigenvalue m_i can be found along any of the high symmetry Γ-M or Γ-K directions. The mirror eigenvalues are independent of in-plane momentum direction, and therefore an identified crossing between two bands along e.g. Γ-M can be traced to a second high-symmetry crossing along Γ-K. Similarly, analogous crossings can be found between the same two bands along all intermediate low-symmetry paths, together resulting in a nodal ring which encloses the Γ point. The energetic positioning of the gapless crossings is not constrained, and thus generically differs between the two in-equivalent high-symmetry directions. The nodal rings thus take on a crown-like appearance in (k_x, k_y, E) space, as illustrated in Fig. 1b. This applies to all nodal rings in the k_z=0 plane of bulk hcp Co(0001).

In the $\frac{\pi}{c}$ or A-containing plane ((k_x, k_y, k_z = 1/2) in fractional coordinates), the situation is different. Each band has its degeneracy doubled along the high-symmetry momentum paths relative to the Γ-containing plane. Notably, though, there is a single two-dimensional co-representation for electronic states along the high-symmetry line joining A = (0, 0, 1/2) and L = (1/2, 0, 1/2). Therefore, all bands along this direction are doubly degenerate, but this degeneracy is lifted when moving outside this path to a generic point in the A-containing plane (k_z=$\frac{\pi}{c}$). This implies that the twofold degeneracy corresponds to a mirror symmetry-protected crossing of two bands, which gives rise to a nodal line along the A-L direction. This second category of nodal line, schematized in Fig. 1c (which is of type-I here) is thus one dimensional, though free to disperse in energy along the A-L direction. Perpendicular to the A-L direction, it forms a Dirac cone-like structure as the degeneracy is reduced. If such a nodal line crosses the Fermi level, it produces a chain-like Fermi surface with nodes at k-vectors where the nodal line is exactly at the Fermi energy. This is schematized with orange dashed lines in Fig. 1c. This space group is equivalent to that of Fe_3GeTe_2, and therefore one could expect to induce small SOC gaps through forceful misalignment of spin- and orbital-angular momentum[2].

For a magnetisation perpendicular to the $c-$ axis ([$1\bar{1}00$]), both of these types of nodal features are severely augmented. In this case, the symmetry is given by the magnetic space group Cm'cm' (No. 63.464). Because the local magnetic moments transform as a pseudo-vector, $\{m_{001}|0, 0, 1/2\}$ is not a symmetry and the protection mechanism for either nodal features in the Γ- and A-containing planes (Fig. 1b, c, respectively) is absent, leading to a gapping of all nodal crossings on these planes. However, in the k_z=0 plane, isolated crossing points can be maintained along a subset of the now-inequivalent Γ-M directions, thus transforming a continuous nodal line into isolated, twofold degenerate, Weyl-like nodal points. For the $k_z = \frac{\pi}{c}$ plane, bands on the A-L line are still doubly degenerate, but this degeneracy is no longer lifted for generic points (k_x, k_y, 1/2) away from this line, and thus X-shaped features can no longer be expected in the

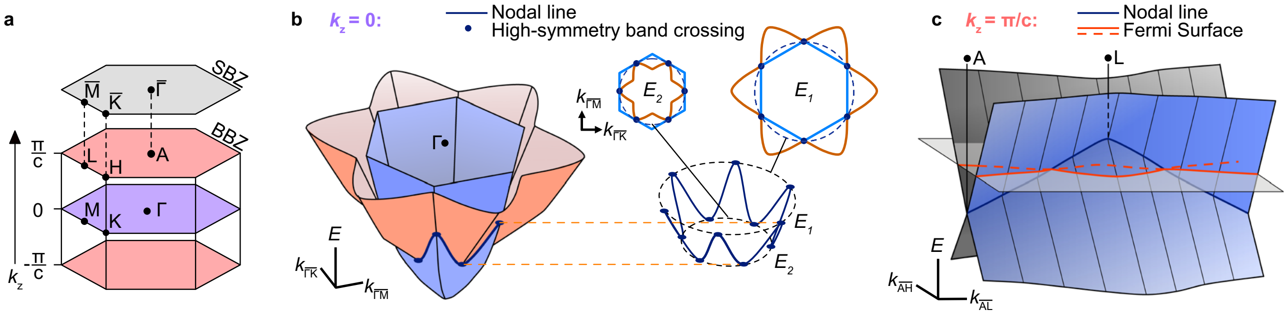

Fig. 1 | Brillouin zones and nodal features of hcp cobalt. **a** bulk (BBZ) and surface (SBZ) Brillouin zones of hcp cobalt with high-symmetry planes and high-symmetry points indicated. **b** Schematic of a nodal-line feature permitted to exist in the $k_z = 0$ plane of hcp cobalt. The nodal line (dark blue solid line) is formed at the intersection of two bands in orange and blue colouring, and encloses the Γ point. The inset demonstrates the energy dispersion of the nodal-line feature. **c** Schematic of the type of nodal line permitted to exist in the $k_z = \pi/c$ plane of hcp cobalt. The nodal line, formed at the intersection of two quasi-linear bands, is present along the entire A-L direction, but free to disperse in energy. Orange lines show the fermiology of such a feature for a Fermi level-positioning indicated with a gray rectangle.

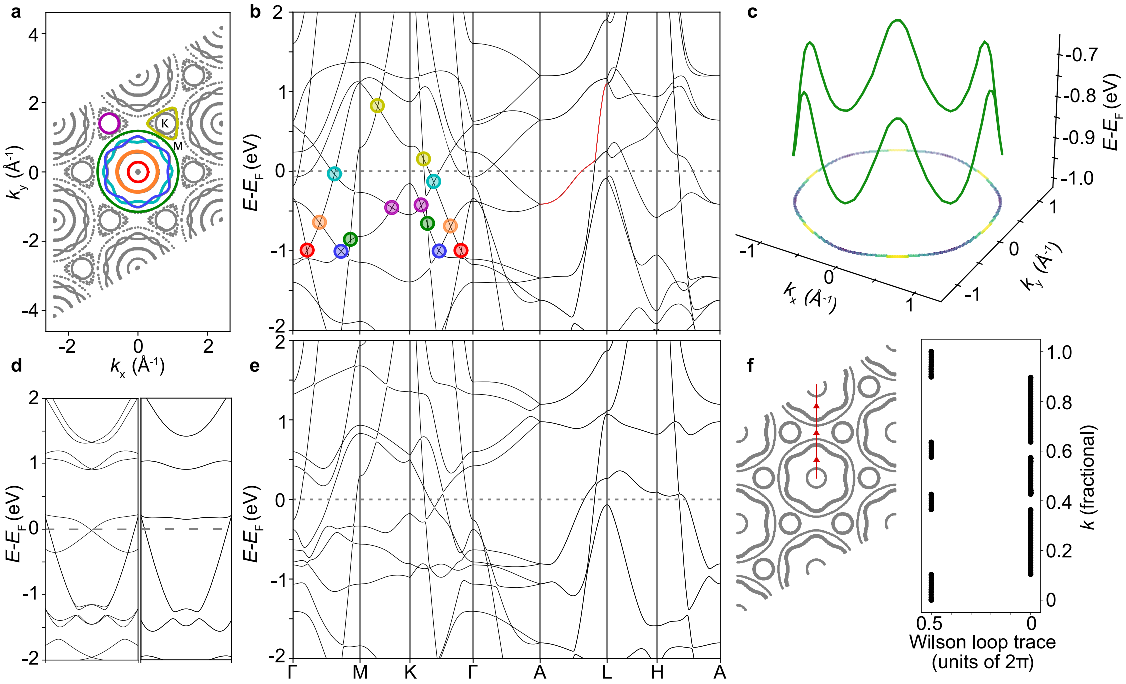

Fig. 2 | Characterization of nodal lines from DFT calculations. **a** Calculation of all nodal points within a window of 2 eV around the Fermi energy at the $k_z = 0$ plane for the magnetic space group P6$_3$/mm'c'. A selection of nodal lines are highlighted with colored lines. **b** DFT band structure calculation for magnetic space group P6$_3$/mm'c', where the circles mark the intersection between the high-symmetry path and the nodal lines in (a). The red-coloured band marks a nodal line which extends along the A-L direction and closes due to boundary conditions. **c** Energy dispersion (green line) of the green-coloured nodal line in (a) and its projection onto the (k_x, k_y) plane (the line colour indicates energy). **d** Dispersion perpendicular to the A-L direction centered at the wave vector where the nodal line, marked in red in (b), crosses the Fermi level for the magnetic space groups P6$_3$/mm'c'(left) and Cm'cm' (right). In the latter case, the band no longer forms a nodal line because symmetry forbids the splitting of the double degeneracy along the A-L direction on the (k_x, k_y, 1/2) plane. **e** Full DFT band structure calculation for magnetic space group Cm'cm'. **f** Characterization of the nodal lines shown in (a) via Wilson loop analysis. The discontinuities in the Wilson loop trace arise when the red path intersects a nodal line, explicitly confirming nodal features in this system.

perpendicular momentum directions. In other words, the nodal lines along the A-L direction vanish for a magnetization strictly parallel to the surface.

Theoretical classification of nodal band features

In Fig. 2a–f, through DFT band structure calculations we identify all nodal ring and nodal-line features near the Fermi level in hcp cobalt. Figure 2b, e display the calculated electronic structure including SOC for both magnetic space groups P6$_3$/mm'c' (Fig. 2b) and Cm'cm' (Fig. 2e). High-symmetry paths in the $k_z = 0$ plane (here Γ-M-K-Γ) result in a gapless node (of either type-I or type-II) for a significant proportion of the total band crossings, due to the mirror eigenvalue m_i acting as the sole differentiator, thus sorting all bands into two irreducible representations.

These mirror-protected band crossings, found by using the Wannier tight-binding model to compute all the crossing points between the n-th and $(n+1)$-th band for all high-symmetry crossings around the Fermi level, are indicated with coloured markers on the left hand side of Fig. 2b. Crossings sharing a marked colour are between the same two bands along different high-symmetry paths. Together, coupled with the C_3 lattice symmetry, they produce band features of the type schematized in Fig. 1b. This is shown explicitly in Fig. 2a, c, which display energy-integrated and energy-resolved $k_x - k_y$ contours ($k_z = 0$) for these crossing points. Note that nodal rings can enclose K instead of Γ, as it is true for the nodal ring connecting high-symmetry band crossings along M-K and Γ-K, shown in purple colour.

Compare this picture to the magnetic space group 63.464 (Cm'cm') (Fig. 2e), where most crossing points are gapped by SOC. In this case, the significant band renormalization and altered symmetry constraints preclude making a direct one-to-one correspondence between bands across these calculations. In Supplementary Fig. 1, we compare the electronic structures of all Γ-M and Γ-K directions for this second magnetic space group. Note how, along the high-symmetry momentum direction corresponding to the real space magnetisation axis, labeled Γ-M$_3$, gapless crossings are maintained despite the change of symmetry. These are therefore isolated protected crossing points, i.e. doubly-degenerate Weyl-like nodes.

The second type of nodal feature, schematized in Fig. 1c, is stabilized in the magnetic space group P6$_3$/mm'c' in the $k_z = \frac{1}{2}$ plane (here A-L-H-A). Of these nodal lines that span the entire A-L direction, one crosses through the Fermi level, indicated with a red line in Fig. 2(b). If not for the SOC gaps forming along all other high-symmetry lines in the $k_z = \frac{1}{2}$ plane, these A-L nodal lines would form part of a nodal surface similar to those found in some non-magnetic systems[9,23,46]. Note that, like the continuous nodal lines in the k_z=0 plane, these nodal-line features are continuous due to the periodic boundary conditions of the BBZ. A low-symmetry band dispersion taken perpendicular to this A-L direction, at the k-vector where the nodal line in red colouring is at the Fermi level, is displayed in the left-hand side of Fig. 2d. The Weyl-like linear band dispersions can be clearly seen, in line with the three-dimensional schematic in Fig. 1c. This is compared to the same band dispersion but for the magnetic space group Cm'cm'. Here, the bands remain doubly degenerate away from the high-symmetry line, and therefore Dirac-like band dispersions collapse into twofold degenerate parabolic dispersions. Consequently, this latter configuration does not show any nodal lines in the A-containing plane. As a point of interest, we note that the other crossing points shown on the left-hand side of Fig. 2d are part of similar A-L nodal lines, but the band dispersion away from $k_{\parallel} = 0$ is more quadratic in appearance. Higher-order nodal lines have been predicted for TiF$_3$, but not thought to be compatible with the magnetic space group of hcp Co where nodal lines can arise[34].

To further confirm that a feature is indeed a symmetry-protected nodal crossing, we perform Wilson loop calculations $W_{k_z}(k_y)$ along k_z over k_y paths. The trace of $W_{k_z}(k_y)$ is quantized to 0 or π and shows a discontinuity

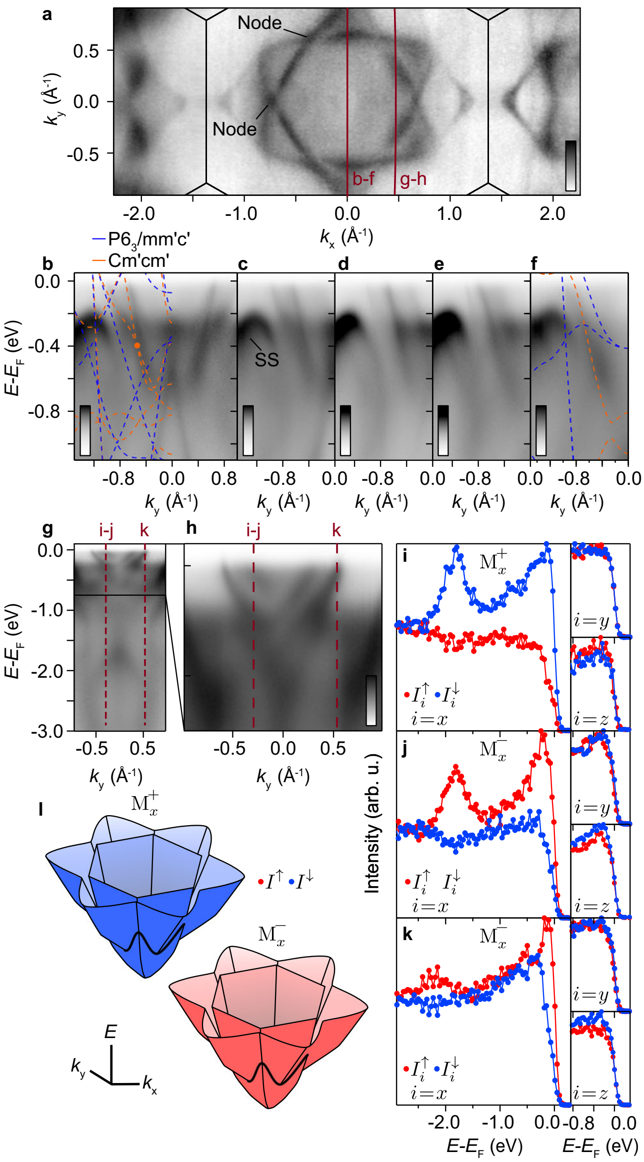

Fig. 3 | Spin-resolved electronic structure of $k_z = 0$ nodal lines in ferromagnetic hcp cobalt. **a** Fermi surface for $k_z = 0$ and hν = 70 eV. Band crossings forming part of a nodal ring feature are indicated. Red lines indicate the k-paths for band dispersions shown in (**b**–**f**) and (**g**, **h**). **b**–**f** Series of $\overline{\Gamma} - \overline{K}$ band dispersions for hν = 70 eV (Γ-containing plane), 72, 78, 85 and 98 eV (A-containing plane) from left to right. The overlaid lines are DFT calculations, with colouring corresponding to the indicated magnetic space group. A nodal point, continuously connected to those in (**a**), is indicated with an orange circle in (**b**). A surface state (SS) feature is labeled. **g, h** Band dispersions along the momentum path indicated in (**a**). **i,k** Three-component spin-resolved energy distribution curves (spin-EDCs) at the k-points indicated in (g, h) ($h\nu$ = 70 eV). The applied magnetization direction is also indicated. **l** Schematic summarizing our findings: The interlocking bands forming the magnetic nodal line carry the same spin-polarisation, fully reversible with applied magnetisation.

when a nodal line is intercepted[47]. The corresponding calculation for the nodal line indicated in Fig. 2c is shown in Fig. 2f, where the two additional nodal lines are confirmed.

Spin-resolved photoemission of nodal rings in k_z = 0 plane

In order to gain further insight into the stabilisation of the nodal band features, in Figs. 3 through 5 we perform photoemission experiments on remanently magnetised bulk hcp Co(0001) following the application of external magnetic field pulses. It is important to note that, while the two magnetic space groups characterized in the previous section are distinct in our theoretical calculations, the experimental reality is more nuanced. Experimentally realized cobalt films (see Methods for growth details) have a canted magnetization, $M(x, y, z)$, with predominantly in-plane magnetic anisotropy $A(x, y) > A(z)$[48,49]. The resulting hysteresis loops are therefore perfectly square neither along the out-of-plane direction nor the direction parallel to the surface. A similar situation is found for bulk Co(0001) single crystals with predominantly out-of-plane magnetic anisotropy $A(z) > A(x, y)$[50].

The projection of the magnetization, $M(x, y, z) = \sqrt{(M(x, y))^2 + (M(z))^2}$ along z originates from the magnetocrystalline anisotropy, leading to electronic bands with $\pm S_z$, while the projections of the magnetization $M(x, y)$ originate from the shape anisotropy, leading to electronic bands with $\pm S_x, \pm S_y$. The magnetocrystalline anisotropy energy is given by the average energy difference between bands in the two configurations (Fig. 2b, e), modifying the dispersion of each band individually[42]. This is a purely relativistic effect which influences the impact of SOC locally within the electronic band structure depending on the orientation of the magnetisation[42]. Altogether, this results in a experimentally measured band structure which derives from a superposition of the two magnetic space groups. Note also that the C_3 symmetry of the SBZ provides three possible in-plane magnetisaiton axes which become inequivalent in the remanent magnetic state, leading to a total of four contributions to the measured electronic structure. In experiment, therefore, as will be shown below, bands belonging to the P6$_3$/mm'c' magnetic space group (Fig. 2a–c), persist even following the application of magnetic field pulses along [1$\overline{1}$00] (see Methods), with their spin-polarisations not locked to the z direction.

In Fig. 3, we focus on nodal features of the classification illustrated in Fig. 1b, i.e. nodal rings within the k_z = 0 (Γ) plane. Figure 3a displays the experimentally obtained Fermi surface of hcp Co for a photon energy of 70 eV, corresponding to $k_z \approx 0$. Most prominent is an interlocking 'flower'-like pattern centered at the Brillouin zone center, with additional arrow-like features towards the M points. The flower-like Fermi surfaces are signatures of the nodal ring, schematized in Fig. 1b and predicted explicitly in Fig. 2.

In Fig. 3b, a band dispersion taken along the k_y direction (parallel to K-Γ-K of the BBZ) is displayed and overlaid with calculations for both the P6$_3$/mm'c' and Cm'cm' magnetic space groups from Fig. 2, with gapless nodes within the flower-like Fermi pockets indicated in Fig. 3a. Despite difficulties in accurately modeling strongly-correlated ferromagnetic 3d transition metals[41,43], there is excellent agreement between experiment and theory with all bulk bands accounted for by the combination of the two theoretical configurations. Most clearly, the steep cone-like feature centered at $k_y = 0$ is captured by the P6$_3$/mm'c' calculation, while the pair of bands which develop a large momentum separation at the Fermi level are well captured by the Cm'cm' calculation. The remaining band, forming a local maxima at approximately -1.2 Å^{-1}and -0.25 eV below the Fermi level is a surface state that threads through the nearby local bandgap.

In Fig. 3c–f, we explore the photon energy dependence of the energy-momentum dispersion along the $\overline{K} - \overline{\Gamma} - \overline{K}$ direction of the SBZ. In photoemission experiments, the photon energy alters the nominal k_z plane[51], with 70 and 98 eV photons found to correspond to the high-symmetry k_z=0 and $\frac{\pi}{c}$ planes respectively, though due to the finite electron mean free path perpendicular to the surface there is significant k_z broadening[51] (see Supplemental Fig. 3 and related discussion in the Supplemental Materials). These dispersions confirm the two-dimensional nature (i.e. non-dispersive behavior along k_z) of the surface state, while demonstrating explicitly the doubling of bulk band degeneracies when approaching the A-containing plane (Fig. 3f), in agreement with the results displayed in Fig. 2.

The indicated gapless node along the Γ-K direction in Fig. 3b at ≈ 400 meV below the Fermi level, is best captured by the DFT calculations for the magnetic space group Cm'cm'. In this case, the nodal ring schematized in Fig. 1b is replaced with isolated gapless nodes along a subset of the high-symmetry directions within the k_z=0 plane (Supplementary Fig. 1). The two inequivalent Γ-K directions both host a gapless node, though no such node exists along any of the three Γ-M directions. While the DFT calculations along the Γ-K direction well-reproduce the experimentally observed band crossing, its behavior with changing azimuthal direction (i.e. rotations within the $k_x - k_y$ plane about the k_z axis) is not reproduced. Experimentally, the pair of bands forming the nodal crossing along Γ-K separate in momentum towards the Fermi level. On the Fermi surface (Fig. 3a), this pair of bands recombine with azimuthal rotation thus forming a second, high-symmetry node along the Γ-M direction and at the Fermi level. This observed connectivity between such energy-offset high-symmetry nodes along the Γ-K and Γ-M directions produces a nodal ring feature exactly as schematized in Fig. 1b. In DFT for the Cm'cm' magnetic space group, however, the observed nodal ring does not form. Instead, the momentum separation between the pair of bands along Γ-K at the Fermi level increases with azimuthal rotation, precluding a high-symmetry crossing along Γ-M. The resulting Fermi surface, not matching the experimental picture, is shown in Supplementary Fig. 2. Therefore, while the band crossing along Γ-K is well described by calculations for the Cm'cm' magnetic space group wherein nodal rings cannot form, the behavior of these bands more generally, and the formation of the observed nodal ring, match only to the $P6_3$/mm'c' magnetic space group. Altogether, the overall agreement to the theoretical calculations and the clear experimental identification of these nodes unambiguously confirms the presence of nodal lines in the k_z=0 plane of hcp Co.

The remainder of Fig. 3 concerns the spin-polarisation of the experimentally confirmed nodal points and the connective band structure forming the Fermi flower. Spin-ARPES measurements were carried out following the application of external magnetic field pulses along [1$\bar{1}$00]. The ability to invert the direction of the magnetic pulses allows to reverse spin-polarisation of magnetic origin, thus disentangling any spin polarisation originating from TRS-preserving mechanisms. Note that such reversal of the spin-polarisation is not possible in conventional non-magnetic nodal-line systems.

In Fig. 3g, h, band dispersions are displayed along the direction parallel to Γ-K at non-zero k_x. The maroon-coloured solid line in Fig. 3a shows this positioning. The dashed lines in Fig. 3g, h indicate the momenta at which spin-resolved energy distribution curves (spin-EDCs) are taken. Note that these two positions are not symmetric about $k_y = 0$. These spin-EDCs, displayed in Fig. 3i, k, show how both bands composing the Fermi flower, along with the bands at much deeper binding energy (Fig. 3g), are strongly spin-polarized in the x-channel (parallel to the Γ-M direction along which the magnetic field pulses were applied). There is also significant S_z spin polarisation, though the S_y (radial) component of spin is negligible. By comparing Fig. 3i, j), it can be clearly seen that the spin-polarisation fully reverses when reversing the direction of the applied magnetic field pulses. Moreover, Fig. 3j, k) together show that the measured spin polarisation retains the same sign when moving from $-k_y$ to $+k_y$ for the same pulse polarity. This information is sufficient to determine that the spin vectors of the bands forming the Fermi surfaces around the Γ point are uniformly aligned, and thus the mirror-symmetry protected nodal points identified along Γ-K and Γ-M are crossings between bands with the same spin-polarisation, consistent with the minority spin manifold of hcp cobalt, and their assignment as TRS-broken Weyl-like nodal lines. This is illustrated schematically in Fig. 3l.

Nodal lines in $k_z = \frac{\pi}{c}$ plane

Next, we search for Weyl-like nodal lines of the type schematisized in Fig. 1c, which can exist along the A-L line in the $k_z = \frac{\pi}{c}$ (A) plane of the BBZ as shown in the calculations in Fig. 2b, d. Figure 4a compares the Fermi surfaces for the two high-symmetry planes in k_z. Consistent with the photon energy dependent band dispersions shown in Fig. 3b–f, the pair of interlocking Fermi surfaces discussed in the previous section has its degeneracy doubled in the $k_z = \frac{\pi}{c}$ plane, thereby transforming into a single Fermi surface. The set of 'arrow'-like features, pointing towards the $\overline{M}$ points at ≈ ± 1.4 $Å^{-1}$is present in both k_z planes. An arc-like feature connecting the heads of the arrow-like features has more prominent spectral weight in the A-containing plane, though the spectral weight of the arrow-like states themselves is lower. As we will demonstrate in the following, these arrow-like states at the Fermi level are signatures of a nodal line spanning the entire A-L-A direction, which are visible in photoemission experiments for both choices of photon energy due to significant k_z broadening and the drift of the nominal k_z plane with increasing k_x (see Supplemental Fig. 3).

Figure 4b displays the calculated Fermi surfaces corresponding to the $P6_3$/mm'c' magnetic space group. Though the size and numbers of Fermi surface features differ, the calculated Fermi surfaces contain qualitatively identical features; namely the presence of 'arc'-like states connecting arrow-like apexes of hexagonal-Fermi sheets.

Crucially, this fermiology, present in both theory and experiment, is characteristic of type-I nodal lines as schematized in Fig. 1c. In Supplemental Fig. 2, the evolution of the calculated Fermi surfaces for both high-symmetry k_z planes with changing binding energy is shown, aiding comparison with the schematics of both types of nodal line features in Fig. 1.

In Fig. 4c, a series of energy-momentum dispersions along the k_y direction for different k_x values are displayed. For each of these spectra, a cone-like feature exhibiting a quasi-relativistic linear dispersion is clearly present, with the gapless node dispersing in energy with changing k_y. As illustrated in the schematic diagram in Fig. 1c, towards the $\overline{\Gamma}$ point (i.e. low or high k_x in Fig. 4c), the bands crossing the Fermi level are the upper legs of the cone-like feature (labeled UL in Figs. 4a, b, g). As the cone disperses towards the $\overline{\mathrm{M}}$ point (intermediate k_x in Fig. 4c), the nodal line crosses the Fermi level to produce the gapless intersections along $k_y = 0$ between bands on the Fermi surface. Beyond this point, the lower legs of the cone-like feature (labeled LL) now form the Fermi surface to produce the arc-like features in Fig. 4a, b. This fermiology is a hallmark of one-dimensional type-I nodal lines which disperse through the Fermi level. In Supplemental Fig. 4, an equivalent dataset to that in Fig. 4c is shown for 98 eV photons.

In Fig. 4d, e, band dispersions are shown along the k_x direction for photon energies nominally probing the Γ- and A-containing planes. Consistent with the comparisons between Fermi surfaces for these two photon energies (Fig. 4a), there are only subtle differences between these band dispersions. The overlays in Fig. 4d, e show how the experimental band dispersion most strongly matches the calculations corresponding to the $P6_3$/mm'c' magnetic space group. Indeed, the experimental observation of conical features can only be reconciled with this magnetic space group, as the upper and lower legs of the band dispersion remain energy degenerate for the Cm'cm' magnetic space group (Fig. 2d).

In Fig. 4f, an additional energy-momentum dispersion is displayed along the k_y direction for the k_x position indicated by the vertical solid line in Fig. 4e. The vertical dashed lines in the dispersion of Fig. 4f highlight the positioning of the spin-EDCs displayed in Fig. 4h–j. As for the spin-EDCs in Fig. 3, the measurements are taken in remanence following the application of an external magnetic field pulse. The spin-EDCs, sampled approximately symmetrically about k_y=0 and for opposite remanent magnetisation directions, show finite spin signal in the x (parallel to the applied magnetization) and the z channels. The y-component of spin (not shown) was again negligible. There are three distinct peaks in the spin-EDCs: the shallowest and deepest of these three peaks correspond to the upper and lower legs of the conical feature, while the middle peak corresponds to a surface state similar to that shown in Fig. 3b. This surface state has suppressed spectral weight at $k_y = 0$, but dominant spectral weight at higher k_y values, where the state is visible approximately 0.3 eV below the Fermi level for all displayed k_x. Its dispersion for intermediate k_y values is seemingly dependent on the energetic positioning of the node: Where the node is near or above the Fermi energy (e.g. k_x=1.36 $Å^{-1}$), the surface state disperses to shallower binding energy towards k_y=0. Conversely, where the node is at high binding energy (e.g. k_x=1.02 $Å^{-1}$), the surface state instead disperses towards deeper binding energy. The origin of this surface state is thus likely related to the nodal line itself, similar to the spin-degenerate (in the absence of SOC) surface states found in a number of non-magnetic nodal-line systems[34,35,37,47,52,53] and the spin-polarised surface state reported in magnetic Co_2MnGa[40].

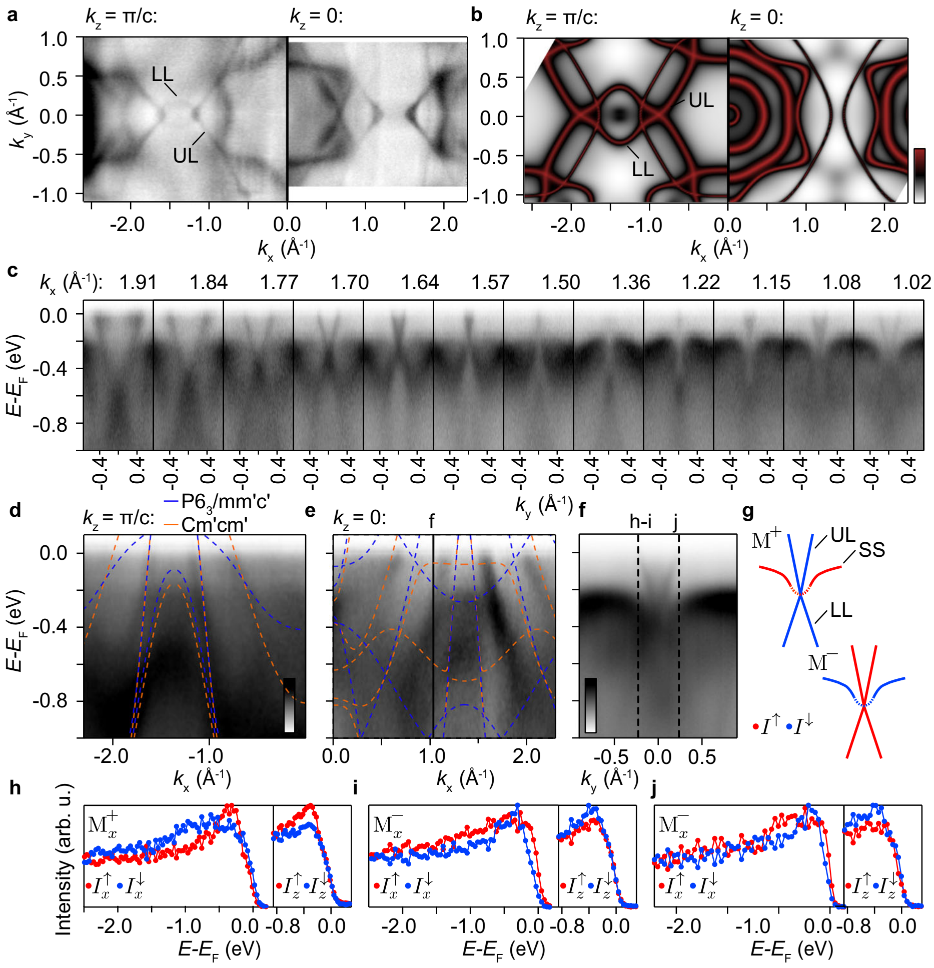

Fig. 4 | Fermi-crossing nodal line along A-L-A. **a** Fermi surfaces at $h\nu$=98eV (left) and 70 eV (right). The nodal features are visible in both high-symmetry planes due to k_z broadening. The Fermi surfaces created by the upper and lower legs (UL and LL, respectively) of the conical features in **c** are indicated. **b** Equivalent Fermi surfaces as generated by density functional theory (DFT) for the 194.279 (P6$_3$/mm'c') magnetic space group of Co. There is strong qualitative agreement to theory. **c** Series of band dispersions (hν = 70 eV) along the k_y direction for the indicated k_x values. Conical features are visible for all choices of k_x. Band dispersions along k_x for both 98 eV (**d**) and 70 eV (**e**) photons. Overlaid dashed lines are DFT calculations for the two magnetic space groups indicated. **f** Band dispersion along k_y for the k_x position indicated in **e**. Dashed lines indicate the positioning of spin-resolved energy distribution curves indicated in **h**–**j**. **g** Schematic summarizing the spin-EDCs in **h**-**j**. **h**–**j** Spin EDCs (hν = 70 eV) for the x and z components at the positions indicated in **f**. The applied magnetisation direction is also indicated.

As is true for the magnetic nodal line in Fig. 3, the signs of the spin-polarisation of the upper and lower branches of the conical features are the same, and thus the twofold-degenerate crossing points are themselves spin-polarised. The surface state has opposite spin-polarisation to the conical feature. All signals remain the same when comparing time-reversal symmetric k-vectors, and reverse controllably when switching the magnetisation polarity. The experimental observation is summarized in the sketch shown in Fig. 4g.

It is important to note that spin-dependent electron-electron interactions contribute to a significant enhancement of lifetime broadening at higher binding energies[43,54]. This makes characterizing magnetic nodal lines at higher binding energy, predicted to exist by the calculations in Fig. 2, difficult spectroscopically due to the quenching of majority spin excitations. Nevertheless, there are still signatures of deeper lying nodal features. Figure 5 provides experimental evidence for a second A-L-oriented nodal line at higher binding energies. A-L band dispersions in the $k_z = \frac{\pi}{c}$ plane (Fig. 5a) clearly demonstrate two nodal-line features (labeled NL1 and NL2), with very similar band dispersions, separated by approximately 0.5 eV. In-plane energy-momentum dispersions taken perpendicular to A-L (Fig. 5b–c) show conical features with a similar energetic separation. Figure 5d–g show constant-energy contours at different binding energies as indicated by horizontal dashed lines in Fig. 5a. These demonstrate how the signatures of both nodal-line features together form complex shapes in the $k_x - k_y$ plane. We note that all experimentally observed nodal lines in Figs. 3–5 are within the minority spin manifold. The energy and spin-dependent correlations, which contribute to the broadening of the deeper lying nodal line in Fig. 5, entirely preclude experimental verification of the majority spin partners of each of these states.

Other systems

To finalise, we briefly consider the application of our findings to other systems. For instance, elemental Zr (space group 194) was previously predicted to host fourfold degenerate analogues of the nodal-line features shown in Fig. 1b, c (the latter forming part of a nodal surface)[46]. The nodal lines in the $k_z = 0$ plane are stabilized by two independent protective mechanisms, mirror symmetry and the combination of inversion and time-reversal symmetries, the latter of which is absent in cobalt. The fourfold degenerate nodal surface in the $k_z = \frac{\pi}{c}$ plane is stabilized by a combination of the non-symmorphic S_{2z} and time-reversal symmetries. Unlike with cobalt, however, for both types of nodal features there is no protection against SOC and thus all nodal lines are gapped everywhere in momentum space. Similar nodal lines with SOC-induced gaps have been found in other non-magnetic 194-space group systems[55], including Cu$_2$Si[56], XTiO$_2$ (X = Li, Na, K, Rb)[57], Zr$_3$Z (Z = Al, Ga, In)[58], TiTe[59], Ti[60] and NiSe[61].

Returning to systems in which TRS is absent, Fe$_3$GeTe$_2$ shares the magnetic space group in which the ungapped nodal-line features in cobalt are stabilized. In that system, perturbations to the magnetisation axis direction are found to gap nodal lines to generate sources and drain of Berry curvature to produce an anomalous Hall effect[2]. Similar arguments should hold for hcp cobalt. More generally, the high number of nodal features found in cobalt is a natural consequence of highly-constrained symmetry arguments in the high-symmetry Brillouin zone planes of a magnetic space group. The hcp lattice of Co is not a necessary prerequisite for this, and indeed similar arguments should apply to fcc Co and other 3d ferromagnetic transition metals[62]. Indeed, a recent prediction of Weyl points and nodal lines in bcc Fe[63] could fall within the framework outlined here. This generality is key to exploring the impact on the electronic structure of spin-

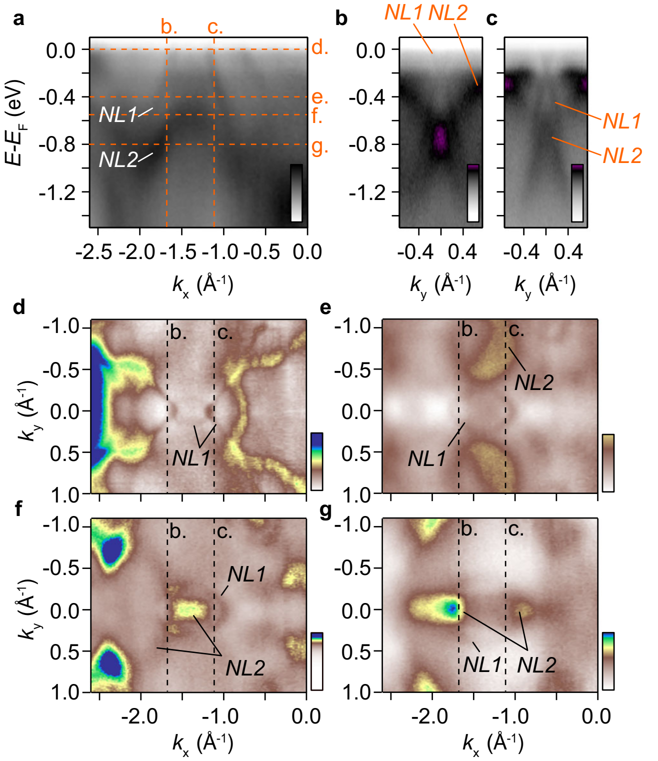

Fig. 5 | Additional nodal-line feature in the $k_z=\frac{\pi}{c}$ plane. a $\bar{\Gamma}-\bar{\mathrm{M}}$ band dispersions (hν = 70 eV) showcasing the previously discussed A-L aligned nodal line (NL1) and a second nodal-line feature at higher binding energy (NL2). Vertical orange dashed lines indicate the k_x positioning of the k_y-aligned band dispersions in (**b**) and (**c**). Horizontal orange dashed lines indicate the binding energies from which the k_x-k_y contours in (**d**–**g**) are extracted. **b, c** Band dispersions perpendicular to $\bar{\Gamma}-\bar{\mathrm{M}}$ at two different non-zero k_x values, each showing two gapless conical band features belonging to the NL1 or NL2 nodal lines. **d–f** Constant-energy k_x-k_y contours for the energies indicated in (**a**). Features belonging to NL1 and NL2 are indicated. Vertical black dashed lines indicate the positioning of the band dispersions in (**b**, **c**).

dependent electron correlations by changing the 3d band filling as a route for investigating the interplay between topology and strong correlations, including the influence of reducing dimensionality[43,64].

Conclusions

In conclusion, through density functional theory and spin- and angle-resolved photoemission, we have established hcp cobalt as host of numerous magnetic nodal-line features within its electronic structure, including at the Fermi level. These features, robustly present at room temperature, possess associated surface states which, similar to the nodal lines themselves, exhibit fully reversible spin textures and are therefore highly relevant for spintronic applications. Cobalt has long been regarded as a prototypical ferromagnet with a well-understood band structure studied for over 40 years[65], yet these findings reveal new fundamental insight into its electronic properties. More generally, the findings outlined here add Co to the overgrowing list of elemental systems with topological band features[66–72], consistent with predictions that one quarter of all naturally occurring solids have topologically non-trivial band crossings[73–75].

Methods

Sample preparation

Hexagonal close-packed (hcp) Co(0001) films were prepared by epitaxial growth of > 20 monolayer (ML) Co on W(110) by evaporation from high purity wires using electron bombardment. The films were crystallized by post-annealing during 5 min at 400 °C. The high structural quality of the films was verified by low-energy electron diffraction. The W(110) substrate was cleaned before deposition by several cycles of annealing in oxygen atmosphere (1×10^{-7} mbar) at 1200 °C followed by flashing at 2200 °C.

Photoemission experiments

Spin-ARPES and ARPES measurements were carried out using p-polarised synchrotron light of energies between 70 and 98 eV at the U125-PGM beamline of BESSY-II in Helmholtz Zentrum Berlin. Photoelectrons were detected with a Scienta R4000 analyzer at the Spin-ARPES endstation, and the base pressure of the experimental setup was better than 10^{-10} mbar. Spin resolution was achieved using a Mott-type spin polarimeter operated at 25 kV and capable of detecting all three components of the spin polarisation. Spin-resolved energy distribution curves (spin-EDCs) were determined according to

$$I_i^{\uparrow,\downarrow} = \frac{I_i^{\mathrm{tot}}(1 \pm P_i)}{2}, \tag{1}$$

where $i = \{x, y, z\}$, $I_i^{\mathrm{tot}} = (I_i^{+} + I_i^{-})$ and $I_i^{\pm}$ is the measured intensity for the oppositely deflected electrons for a given channel, corrected by a relative efficiency calibration. The final spin polarisation is defined as follows

$$P_i = \frac{I_i^{+} - I_i^{-}}{S(I_i^{+} + I_i^{-})}, \tag{2}$$

where S=0.12 is the Sherman function.

The samples were measured in remanence after applying a pulsed magnetic field of 0.5 T along the $[1\bar{1}00]$ direction.

The spin-resolved spectra were additionally corrected by an experimental symmetry of ≈ 5 percent, determined from consecutive spin-resolved measurements with opposite magnetization directions as in reference[76].

Photon energy to k_z mapping was done by assuming a free-electron final state, and taking an inner potential, V_0, of 14.8 eV, as determined in earlier works[42]. We refer the reader to the Supplementary Materials for further information.

Theoretical calculations

To perform the Density Functional Theory (DFT) calculations, we used the *Vienna Ab-initio Simulation Package* (VASP) software[77,78]. The Projector-Augmented Wave (PAW) pseudo-potentials[79] included the Perdew-Burke-Ernzenhof (PBE) implementation of the Generalized Gradient Approximation (GGA) for the exchange-correlation functional[80]. To account for the correlations of the localized d electrons in Co, we introduced a Hubbard-like repulsive term (DFT+U) in the spherically symmetric approximation[81]. The repulsive parameter was adjusted to U = 2 eV to reproduce the experimentally reported magnetic moment per Co atoms of around 1.8 μB[82]. The energy cutoff of the plane wave basis was set to 600 eV and the **k** point grid was a Gamma-centered, regular Monkhorst-Pack point set of dimensions 11 × 11 × 7 providing a uniform density of points over the first Brillouin Zone. The crystal structure found in the literature[83] was slightly expanded to match the experimentally observed Fermi surfaces. Symmetry classification of the crystal structure and the eigenstates were done with `irrep`[84].

To analyze the nodal lines and perform the Wilson loop calculations, we constructed maximally localized Wannier functions as implemented in Wannier90[85], with a starting basis of s, p, d orbitals per Co atom for a total of 36 Wannier functions, accounting for the doubling due to spin. The bands were frozen in an energy window of 2 eV centered around the Fermi level during the disentanglement procedure to exactly reproduce the bands in that energy range. The Wilson loop trace for a given band considers all bands below the node of interest, including the lower part of the considered crossing. Further calculations were performed using the interpolated Wannier tight-binding (TB) model as implemented in WannierTools[86].

Data availability

Data are available from the authors upon reasonable request.

Received: 7 October 2025; Accepted: 2 January 2026;

References

1. Sánchez-Barriga, J., Clark, O. J. & Rader, O.*Angle-resolved photoemission of topological materials*, vol. 4, 334–369 (Elsevier, Netherlands, 2024), 2nd edn. https://www.sciencedirect.com/science/article/pii/B9780323908009002742.
2. Kim, K. et al. Large anomalous hall current induced by topological nodal lines in a ferromagnetic van der waals semimetal. *Nat. Mater.* **17**, 794–799 (2018).
3. Burkov, A. A. Anomalous hall effect in weyl metals. *Phys. Rev. Lett.* **113**, 187202 (2014).
4. Chang, G. et al. Room-temperature magnetic topological weyl fermion and nodal line semimetal states in half-metallic heusler co2tix (x=si, ge, or sn). *Sci. Rep.* **6**, 38839 (2016).
5. Kim, Y., Wieder, B. J., Kane, C. L. & Rappe, A. M. Dirac line nodes in inversion-symmetric crystals. *Phys. Rev. Lett.* **115**, 036806 (2015).
6. Fang, C., Chen, Y., Kee, H.-Y. & Fu, L. Topological nodal line semimetals with and without spin-orbital coupling. *Phys. Rev. B* **92**, 081201 (2015).
7. Bzdušek, T., Wu, Q., Rüegg, A., Sigrist, M. & Soluyanov, A. A. Nodal-chain metals. *Nature* **538**, 75–78 (2016).
8. Bi, R., Yan, Z., Lu, L. & Wang, Z. Nodal-knot semimetals. *Phys. Rev. B* **96**, 201305 (2017).
9. Fu, B. B. et al. Dirac nodal surfaces and nodal lines in zrsis. *Sci. Adv.* **5**, eaau6459 (2019).
10. Chang, T.-R. et al. Realization of a type-ii nodal-line semimetal in mg3bi2. *Adv. Sci.* **6**, 1800897 (2019).
11. Bian, G. et al. Topological nodal-line fermions in spin-orbit metal pbtase2. *Nat. Commun.* **7**, 10556 (2016).
12. Yu, R., Weng, H., Fang, Z., Dai, X. & Hu, X. Topological node-line semimetal and dirac semimetal state in antiperovskite $\mathrm{cu}_3\mathrm{PdN}$. *Phys. Rev. Lett.* **115**, 036807 (2015).
13. Xie, L. S. et al. A new form of ca3p2 with a ring of dirac nodes. *APL Mater.* **3**, 083602 (2015).
14. Xu, Q., Yu, R., Fang, Z., Dai, X. & Weng, H. Topological nodal line semimetals in the cap$_3$ family of materials. *Phys. Rev. B* **95**, 045136 (2017).
15. Wu, H. et al. Nonsymmorphic symmetry-protected band crossings in a square-net metal ptpb4. *npj Quantum Mater.* **7**, 31 (2022).
16. Yang, S.-Y. et al. Symmetry demanded topological nodal-line materials. *Adv. Phys.: X* **3**, 1414631 (2018).
17. Ekahana, S. A. et al. Observation of nodal line in non-symmorphic topological semimetal inbi. *N. J. Phys.* **19**, 065007 (2017).
18. Wu, Y. et al. Dirac node arcs in ptsn4. *Nat. Phys.* **12**, 667–671 (2016).
19. Li, S. et al. Nonsymmorphic-symmetry-protected hourglass dirac loop, nodal line, and dirac point in bulk and monolayer X_3site$_6$ (x = ta, nb). *Phys. Rev. B* **97**, 045131 (2018).
20. Schoop, L. M. et al. Dirac cone protected by non-symmorphic symmetry and three-dimensional dirac line node in zrsis. *Nat. Commun.* **7**, 11696 (2016).
21. Neupane, M. et al. Observation of topological nodal fermion semimetal phase in zrsis. *Phys. Rev. B* **93**, 201104 (2016).
22. Chen, C. et al. Dirac line nodes and effect of spin-orbit coupling in the nonsymmorphic critical semimetals mSiS(m = Hf, Zr). *Phys. Rev. B* **95**, 125126 (2017).
23. Topp, A. et al. Surface floating 2d bands in layered nonsymmorphic semimetals: Zrsis and related compounds. *Phys. Rev. X* **7**, 041073 (2017).
24. Hosen, M. M. et al. Tunability of the topological nodal-line semimetal phase in ZrSix-type materials (x = S, Se, Te). *Phys. Rev. B* **95**, 161101 (2017).
25. Wang, X. et al. Quantum electronics: Evidence of both surface and bulk dirac bands and anisotropic nonsaturating magnetoresistance in zrsis (adv. electron. mater. 10/2016). *Adv. Electron. Mater.* **2**, 10 (2016).
26. Yen, Y. et al. Dirac nodal line and rashba spin-split surface states in nonsymmorphic zrgete. *N. J. Phys.* **23**, 103019 (2021).
27. Cheng, Z. et al. Visualizing dirac nodal-line band structure of topological semimetal zrgese by arpes. *APL Mater.* **7**, 051105 (2019).
28. Wang, Y. et al. Spectroscopic evidence for the realization of a genuine topological nodal-line semimetal in lasbte. *Phys. Rev. B* **103**, 125131 (2021).
29. Lou, R. et al. Emergence of topological bands on the surface of zrsnte crystal. *Phys. Rev. B* **93**, 241104 (2016).
30. Hirschmann, M. M., Leonhardt, A., Kilic, B., Fabini, D. H. & Schnyder, A. P. Symmetry-enforced band crossings in tetragonal materials: Dirac and weyl degeneracies on points, lines, and planes. *Phys. Rev. Mater.* **5**, 054202 (2021).
31. Xie, Y.-M. et al. Kramers nodal line metals. *Nat. Commun.* **12**, 3064 (2021).
32. Zhang, Y. et al. Kramers nodal lines and weyl fermions in smalsi. *Commun. Phys.* **6**, 134 (2023).
33. Seo, J. et al. Colossal angular magnetoresistance in ferrimagnetic nodal-line semiconductors. *Nature* **599**, 576–581 (2021).
34. Li, Y. Magnetic quadratic nodal lines in half-metallic anode material tif3: A first-principles study. *Phys. B: Condens. Matter* **686**, 416083 (2024).
35. Yang, X. P. et al. A topological hund nodal line antiferromagnet. *Nat. Commun.* **15**, 7052 (2024).
36. Jeon, S., Oh, Y.-T. & Kim, Y. Ferromagnetic nodal-line metal in monolayer *h*-inc. *Phys. Rev. B* **100**, 035406 (2019).
37. Jin, L. et al. Ferromagnetic two-dimensional metal-chlorides mcl (m = sc, y, and la): Candidates for weyl nodal line semimetals with small spin-orbit coupling gaps. *Appl. Surf. Sci.* **520**, 146376 (2020).
38. Schröter, N. B. M. et al. Weyl fermions, fermi arcs, and minority-spin carriers in ferromagnetic cos2. *Sci. Adv.* **6**, eabd5000 (2020).
39. Robredo, I. et al. Theoretical study of topological properties of ferromagnetic pyrite cos2. *J. Phys. D: Appl. Phys.* **55**, 304004 (2022).
40. Belopolski, I. et al. Discovery of topological weyl fermion lines and drumhead surface states in a room temperature magnet. *Science* **365**, 1278–1281 (2019).
41. Sánchez-Barriga, J. et al. Strength of correlation effects in the electronic structure of iron. *Phys. Rev. Lett.* **103**, 267203 (2009).
42. Sánchez-Barriga, J. et al. Quantitative determination of spin-dependent quasiparticle lifetimes and electronic correlations in hcp cobalt. *Phys. Rev. B* **82**, 104414 (2010).
43. Sánchez-Barriga, J. et al. Effects of spin-dependent quasiparticle renormalization in fe, co, and ni photoemission spectra:an experimental and theoretical study. *Phys. Rev. B* **85**, 205109 (2012).
44. Sánchez-Barriga, J., Ovsyannikov, R. & Fink, J. Strong spin dependence of correlation effects in ni due to stoner excitations. *Phys. Rev. Lett.* **121**, 267201 (2018).
45. Campbell, B. J., Stokes, H. T., Perez-Mato, J. M. & Rodríguez-Carvajal, J. Introducing a unified magnetic space-group symbol. *Acta Crystallogr. Sect. A* **78**, 99–106 (2022).
46. Zhang, L. & Wang, K. Pure zirconium: Type ii nodal line and nodal surface states. *Front. Chem.* **8**, 585753 (2020).
47. Chan, Y.-H., Chiu, C.-K., Chou, M. Y. & Schnyder, A. P. Topological semi-metals with line nodes and drumhead surface states. *Phys. Rev. B* **93**, 205132 (2016).
48. Fritzsche, H., Kohlhepp, J. & Gradmann, U. Epitaxial strain and magnetic anisotropy in ultrathin co films on w(110). *Phys. Rev. B* **51**, 15933–15941 (1995).
49. Kleibert, A., Senz, V., Bansmann, J. & Oppeneer, P. M. Thickness dependence and magnetocrystalline anisotropy of the x-ray transverse magneto-optical kerr effect at the Co2*p* edges of ultrathin co films on w(110). *Phys. Rev. B* **72**, 144404 (2005).
50. Mulazzi, M. et al. Fermi surface of co(0001) and initial-state linewidths determined by soft x-ray angle-resolved photoemission spectroscopy. *Phys. Rev. B* **80**, 241106 (2009).
51. Damascelli, A. Probing the Electronic Structure of Complex Systems by ARPES. *Phys. Scr.* **2004**, T109 61 (2004).
52. Hosen, M. M. et al. Experimental observation of drumhead surface states in sras3. *Sci. Rep.* **10**, 2776 (2020).

53. Muechler, L. et al. Modular arithmetic with nodal lines: Drumhead surface states in zrsite. *Phys. Rev. X* **10**, 011026 (2020).
54. Monastra, S. et al. Quenching of majority-channel quasiparticle excitations in cobalt. *Phys. Rev. Lett.* **88**, 236402 (2002).
55. Zhang, J. et al. Topological band crossings in hexagonal materials. *Phys. Rev. Mater.* **2**, 074201 (2018).
56. Feng, B. et al. Experimental realization of two-dimensional dirac nodal line fermions in monolayer cu2si. *Nat. Commun.* **8**, 1007 (2017).
57. Yang, T., Jin, L., Liu, Y., Zhang, X. & Wang, X. Spin-polarized type-ii nodal loop and nodal surface states in hexagonal compounds $x$tio$_2$ (x = li, na, k, rb). *Phys. Rev. B* **103**, 235140 (2021).
58. Xu, H., Xi, H. & Gao, Y.-C. Hexagonal zr3x (x = al, ga, in) metals: High dynamic stability, nodal loop, and perfect nodal surface states. *Front. Chem.* **8**, 608398 (2020).
59. Lin, P., Fang, F., Zhang, L., Li, Y. & Wang, K. Various nodal lines in p63/mmc-type tite topological metal and its (001) surface state. *Front. Chem.* **9**, 755350 (2021).
60. Zhang, X., Jin, L., Dai, X. & Liu, G. Highly anisotropic type-ii nodal line state in pure titanium metal. *Appl. Phys. Lett.* **112**, 122403 (2018).
61. Pradhan, S. et al. Topological nodal line features in nise semimetal: Insights from electronic transport and density functional theory studies. *Phys. Rev. B* **110**, 195153 (2024).
62. Gosálbez-Martínez, D., Souza, I. & Vanderbilt, D. Chiral degeneracies and fermi-surface chern numbers in bcc fe. *Phys. Rev. B* **92**, 085138 (2015).
63. Gosálbez-Martínez, D., Autès, G. & Yazyev, O. V. Topological fermi-arc surface resonances in bcc iron. *Phys. Rev. B* **102**, 035419 (2020).
64. Grechnev, A. et al. Theory of bulk and surface quasiparticle spectra for fe, co, and ni. *Phys. Rev. B* **76**, 035107 (2007).
65. Eastman, D. E., Himpsel, F. J. & Knapp, J. A. Experimental exchange-split energy-band dispersions for fe, co, and ni. *Phys. Rev. Lett.* **44**, 95–98 (1980).
66. Nayak, A. K. et al. Resolving the topological classification of bismuth with topological defects. *Sci. Adv.* **5**, eaax6996 (2019).
67. Schindler, F. et al. Higher-order topology in bismuth. *Nat. Phys.* **14**, 918–924 (2018).
68. Hsieh, D. et al. Observation of unconventional quantum spin textures in topological insulators. *Science* **323**, 919–922 (2009).
69. Clark, O. J. et al. Observation of a giant mass enhancement in the ultrafast electron dynamics of a topological semimetal. *Commun. Phys.* **4**, 165 (2021).
70. Hossain, M. S. et al. A hybrid topological quantum state in an elemental solid. *Nature* **628**, 527–533 (2024).
71. Yan, B. et al. Topological states on the gold surface. *Nat. Commun.* **6**, 10167 (2015).
72. Agapito, L. A., Kioussis, N., Goddard, W. A. & Ong, N. P. Novel family of chiral-based topological insulators: Elemental tellurium under strain. *Phys. Rev. Lett.* **110**, 176401 (2013).
73. Bradlyn, B. et al. Topological quantum chemistry. *Nature* **547**, 298–305 (2017).
74. Vergniory, M. G. et al. A complete catalogue of high-quality topological materials. *Nature* **566**, 480–485 (2019).
75. Vergniory, M. G. et al. All topological bands of all nonmagnetic stoichiometric materials. *Science* **376**, eabg9094 (2022).
76. Sánchez-Barriga, J. et al. Photoemission of Bi_2Se_3 with Circularly Polarized Light: Probe of Spin Polarization or Means for Spin Manipulation? *Phys. Rev. X* **4**, 011046 (2014).
77. Kresse, G. & Furthmüller, J. Efficient iterative schemes for ab initio total-energy calculations using a plane-wave basis set. *Phys. Rev. B* **54**, 11169–11186 (1996).
78. Kresse, G. & Hafner, J. Ab initio molecular dynamics for liquid metals. *Phys. Rev. B* **47**, 558–561 (1993).
79. Blöchl, P. E. Projector augmented-wave method. *Phys. Rev. B* **50**, 17953–17979 (1994).
80. Perdew, J. P., Burke, K. & Ernzerhof, M. Generalized Gradient Approximation Made Simple. *Phys. Rev. Lett.* **77**, 3865–3868 (1996).
81. Dudarev, S. L., Botton, G. A., Savrasov, S. Y., Humphreys, C. J. & Sutton, A. P. Electron-energy-loss spectra and the structural stability of nickel oxide: An lsda$+$u study. *Phys. Rev. B* **57**, 1505–1509 (1998).
82. Moon, R. M. Distribution of magnetic moment in hexagonal cobalt. *Phys. Rev.* **136**, A195–A202 (1964).
83. Černý, M., Pokluda, J., Šob, M., Friák, M. & Šandera, P. Ab initio calculations of elastic and magnetic properties of fe, co, ni, and cr crystals under isotropic deformation. *Phys. Rev. B* **67**, 035116 (2003).
84. Iraola, M. et al. IrRep: Symmetry eigenvalues and irreducible representations of ab initio band structures. *Comput. Phys. Commun.* **272**, 108226 (2022).
85. Mostofi, A. A. et al. An updated version of wannier90: A tool for obtaining maximally-localised wannier functions. *Comput. Phys. Commun.* **185**, 2309–2310 (2014).
86. Wu, Q., Zhang, S., Song, H.-F., Troyer, M. & Soluyanov, A. A. WannierTools: An open-source software package for novel topological materials. *Comput. Phys. Commun.* **224**, 405–416 (2018).

Acknowledgements

J.S.-B. Acknowledges financial support from the Impuls- und Vernetzungsfonds der Helmholtz-Gemeinschaft under grant No. HRSF-0067. M.G.V. and M.G.-D. Thank support to PID2022-142008NB-I00 project funded by MICIU/AEI/10.13039/501100011033 and FEDER, UE, Canada Excellence Research Chairs Program for Topological Quantum Matter, NSERC Quantum Alliance France-Canada and to Diputación Foral de Gipuzkoa Programa Mujeres y Ciencia. This work was supported by the Deutsche Forschungsge-meinschaft (DFG) through QUAST-FOR5249 and the Würzburg-Dresden Cluster of Excellence on Complexity and Topology in Quantum Matter, ct.qmat (EXC 2147, Project ID 390858490). IMDEA team acknowledges support from the Spanish AEI PID2024-157112OB-C53 (HYBRID-OS: HYPERFAN) and from the Comunidad de Madrid through projects TEC-2024/TEC-380 (Mag4TIC-CM).

Author contributions

O.J.C., J.F. and J.S.-B. grew the Co films and performed the photoemission experiments. M.G.-D. and M.G.V. performed the theoretical calculations. O.J.C. and J.S.-B. analysed the data. O.J.C. and J.S.-B. wrote the manuscript with significant contribution from M. G.-D, and further input from J.F., O.R., R.M. and M.G.V. O.J.C. and J.S.B. conceived the project and were responsible for overall project planning and direction.

Funding

Open Access funding enabled and organized by Projekt DEAL.

Competing interests

The authors declare no competing interests.

Additional information

Supplementary information The online version contains supplementary material available at https://doi.org/10.1038/s43246-026-01072-6.

Correspondence and requests for materials should be addressed to J. Sánchez-Barriga.

Peer review information *Communications Materials* thanks Qi Jiang and the other, anonymous, reviewer(s) for their contribution to the peer review of this work. A peer review file is available.